International Journal of Plasticity 179 (2024) 104020

Contents lists available at ScienceDirect

International Journal of Plasticity

journal homepage: www.elsevier.com/locate/ijplas

Understanding the effect of refractory metal chemistry on the stacking fault energy and mechanical property of Cantor-based multi-principal element alloys

Prashant Singh [a,*], William Trehern [b], Brent Vela [c], Prince Sharma [a], Tanner Kirk [c], Zongrui Pei [d], Raymundo Arroyave [c], Michael C. Gao [b], Duane D. Johnson [a,e]

[a] Ames Laboratory, U.S. Department of Energy, Iowa State University, Ames, IA 50011, USA
[b] National Energy Technology Laboratory, 1450 Queen Ave SW, Albany, OR 97321, USA
[c] Department of Materials Science & Engineering, Texas A&M University, College Station, TX 77843, USA
[d] New York University, New York, NY 10012, USA
[e] Department of Materials Science & Engineering, Iowa State University, Ames, IA 50011, USA

ARTICLE INFO

Keywords:
Multi-principal element alloy
CALPHAD
DFT
Stacking-fault energy
Mechanical properties

ABSTRACT

Multi-principal-element alloys (MPEAs) based on *3d*-transition metals show remarkable mechanical properties. The stacking fault energy (SFE) in face-centered cubic (fcc) alloys is a critical property that controls underlying deformation mechanisms and mechanical response. Here, we present an exhaustive density-functional theory study on refractory- and copper-reinforced Cantor-based systems to ascertain the effects of refractory metal chemistry on SFE. We find that even a small percent change in refractory metal composition significantly changes SFEs, which correlates favorably with features like electronegativity variance, size effect, and heat of fusion. For fcc MPEAs, we also detail the changes in mechanical properties, such as bulk, Young's, and shear moduli, as well as yield strength. A Labusch-type solute-solution-strengthening model was used to evaluate the temperature-dependent yield strength, which, combined with SFE, provides a design guide for high-performance alloys. We also analyzed the electronic structures of two down-selected alloys to reveal the underlying origin of optimal SFE and strength range in refractory-reinforced fcc MPEAs. These new insights on tuning SFEs and modifying composition-structure-property correlation in refractory- and copper-reinforced MPEAs by chemical disorder, provide a chemical route to tune twinning- and transformation-induced plasticity behavior.

1. Introduction

Multi-principal-element alloys (MPEAs) or high-entropy alloys (HEAs), in (near-) equal concentrations, take the compositional complexity to a new extreme, where the notion of solutes and solvents breaks down (Miracle et al., 2017; George et al., 2019; Gao et al., 2016; Chang et al., 2020; Tsai et al., 2014). The MPEAs based on several principal elements and driven by configurational entropy of mixing tends to form simple solid solutions such as body-centered cubic (BCC), face-centered cubic (FCC) or hexagonal closed packed (HCP) crystal phases rather than intermetallic compounds (Otto et al., 2013; Senkov et al., 2016; Chen et al., 2023; Zhou et al., 2018),

* Corresponding author.
E-mail addresses: psingh84@ameslab.gov, prashant40179@gmail.com (P. Singh).

https://doi.org/10.1016/j.ijplas.2024.104020
Received 21 March 2024; Received in revised form 2 June 2024;
Available online 4 June 2024

which gives rise to their exceptional mechanical properties such as hardness, strength, high temperature stability, and cryogenic properties (Wu et al., 2014; Deng et al., 2015; George et al., 2020; Tsao et al., 2017; Li et al., 2017; Shi et al. 2019; Yin et al. 2021). Recent advances show rapid development of novel MPEAs for extremely broad spectrum with a clear focus on elevated temperatures such as turbine blades and nuclear applications (Praveen et al., 2018; Yan et al., 2020; El-Atwani et al., 2019; Ouyang et al., 2023).

Notably, the stacking faults (SFs) are the most common defects that largely determine the mechanical property (e.g., plasticity (Xu et al., 2022; Kim et al., 2022; Le et al., 2022) and strength-ductility trade-off (Wei et al., 2022; Wagner et al., 2023; Rao et al., 2018; Li et al., 2023) of FCC metals and alloys, which can be tailored by a number of ways including chemical composition (Khan et al., 2022; Singh et al., 2021). SFs represent an irregularity in the sequence of crystalline planes in a FCC lattice, where the excess energy to create a such faults is represented by the stacking fault energy (SFE). SFs are created during the dissociation of lattice dislocations into partial dislocations to reduce the elastic energy according to Frank's rule (Jia et al., 2021). Typically, the SFE is closely related to the available deformation mechanisms (Anderson et al., 2017). The low SFEs in fcc alloys are often connected to twinning-induced plasticity (TWIP) or transformation-induced plasticity (TRIP) that increases the dislocation storage capacity, tendency of deformation twinning, strain, plasticity, and hardening rate (Grässel et al., 2000). Further lowering of SFE is often connected to fcc-hcp phase transition, resulting in enhanced plasticity through TRIP (Liu et al., 2019). Also, the value of SFE is correlated with the onset of TRIP, TWIP, or slip-dominated plasticity (Zhao et al., 2006), along with plasticity mechanisms in FCC crystals (Huang et al., 2018). Chemical complexity is another aspect that can significantly modify the SFE, which can prominently modify the mechanical behavior (Suzuki et al., 1952, 1962; Freund et al., 2017) and martensitic transformation (Makineni et al., 2018; Zaretsky, et al., 2005).

Refractory metals have been crucial alloying additions in improving the high temperature properties to superalloys (Zaretsky et al., 2005; Ouyang et al., 2024; P. Singh et al., 2024). However, the significance of systematic substitution of refractory metals on SFEs and other mechanical properties of FCC alloys is not well understood. In this work, we focused on investigating the effect of substituting refractories metals, i.e., Nb, Ta, Mo, W, on the SFEs V-Cr-Mn-Fe-Co-Ni-Al (94 compositions) and Cr-Mn-Fe-Co-Ni-Ti-Al-Cu-Mo (122 compositions) MPEAs using first-principles density-functional theory (DFT) calculations. We found that even a small refractory composition addition leads to strong SFE tunability of 3*d*-transition metal MPEAs. The effect of composition change in atomic and alloy features was also analyzed in refractory-reinforced MPEAs. A detailed analysis of SFE calculation from two different models, i.e., (i) axial next-nearest-neighbor Ising (ANNNI) model and (ii) model supercell approach, was discussed to provide rationality behind SFE modeling. The chemical disorder was modeled using the coherent-potential approximation (CPA). The combination of supercells and the CPA makes it possible to investigate arbitrary compositions accurately and to elucidate the impact of tuning the composition of individual elements.

2. Method

CALculation of PHAse Diagram (CALPHAD): To probe the effect of refractory and copper additions on stacking-fault energy, two sets of alloys were down-selected from two distinct alloy spaces based on single-phase stability, higher strength (at 900 K), high-solidus temperature (critical temperature range where alloy is solid), narrow solidification range (important for alloy printability), and higher electronegativity variance (>0.11 for stability and strengthening), which are critically explained in the following sections. The down-selection workflow combining CALPHAD and DFT is shown in Fig.1.

CALPHAD filtering of V-Cr-Mn-Fe-Co-Ni-Al MPEAs: The CALPHAD downselection method used to study refractory additions uses

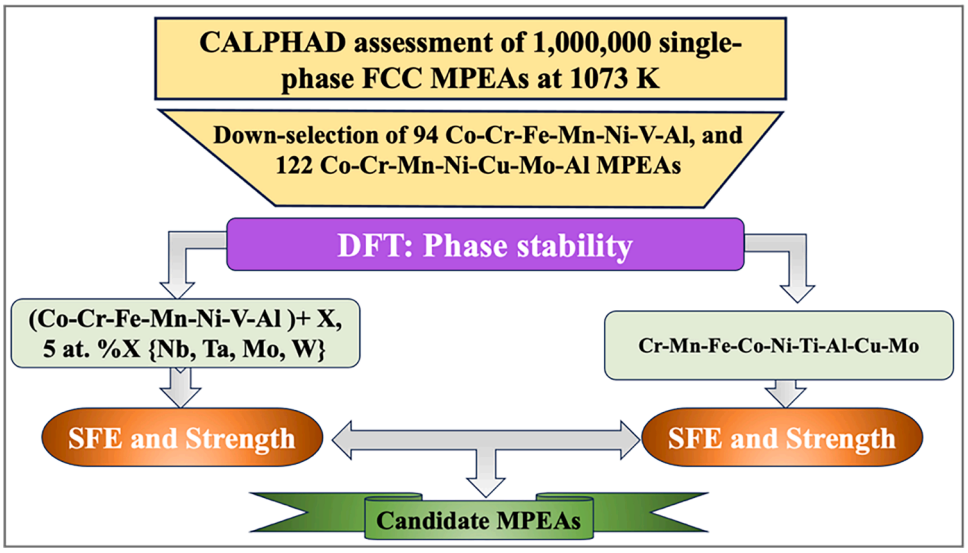

Fig. 1. Alloy selection framework employed in the current work. CALPHAD was employed to down-select a few candidate alloys from a vast composition space by applying constraints on properties like SFE and strength. The SFE calculation was done using high-throughput DFT.

legacy calculations (Khan et al., 2022). The first 1000,000 alloys were randomly sampled from the V-Cr-Mn-Fe-Co-Ni-Al alloy space, which constitute the initial alloy design space. As a first approximation to screen for alloys that likely have single-phase (i.e., no deleterious phases) and high strength at 800 °C with greater than 10 at.% were filtered from the initial design space, leaving 36,294 feasible alloys. The single-phase FCC alloys at 800 °C were identified using Thermo-Calc's Equilibrium module equipped with the TCHEA3 thermodynamic database. These 36,294 alloys were then filtered to identify candidates with a sufficiently high solidus temperature for operation at 800 °C and a sufficiently narrow solidification range (less than 100 °C) to decrease the likelihood of hot cracking during additive manufacturing (Mao et al., 2017; Chen et al., 2018). We stipulate that alloys must have a solidus temperature greater than 1600 K (1327 °C). The threshold of the solidus constraint is set at 1600 K (1327 °C) following the rule-of-thumb that the operating temperature of an alloy should not exceed 2/3rds of its melting point (e.g., $3/2 \times 1073\,K \approx 1600$ K), which resulted into 20, 147 feasible alloys. Finally, a more accurate and expensive Scheil simulation was performed on 20,147 alloys with same constraints that leads to 5739 alloys. Of these 5379 alloys, we downselected around 1.7 % of candidates or 94 compositions based on the CALPHAD criteria of single-phase stability in the fcc phase, higher electronegativity variance (>0.11), solidus temperature, and solidification ranges for further exploration within DFT. Once these 94 candidates were identified, the 5 at.% of either Nb, Ta, Mo, or W were added to the alloys. The remaining elements in the 94 compositions were reduced in equal amounts to accommodate the 5 at.% refractory additions.

CALPHAD filtering of Cu-based MPEAs: Regarding probing the effect of Cu, the selection process for these alloys begins with identifying a set of base elements: Fe, Ni, and Co. Additional elements are added to this base in various combinations to form 11 different alloy systems: Ti, Cr, Al, Mo, Cu, Mn, and Nb. The systems range in complexity, with some containing as few as 4 elements and others containing up to 6. The various combinations of these elements were dictated by expert opinion. These systems are listed in Table 1. These systems were then grid sampled at 5 at.%, resulting in 78,489 candidate alloys. We then stipulate that candidate alloys must contain at least 2 at.% of the addition elements Ti, Cr, Al, Mo, Cu, Mn, or Nb. This reduces the design space to 27755 candidate alloys. These 27755 alloys were then filtered with the same set of constraints used in the first case study, i.e., no Al greater than 10 at.%, single fcc phase stability at 800 °C, a solidification range less than 100 °C, and a solidus temperature of 1600 K. Regarding the constraint on Al content, only 23751 alloys remain after applying this constraint. Regarding the solidification range, only 3752 alloys remain after applying this constraint. Regarding the fcc phase stability, only 493 alloys remain after applying this constraint. The union of these constraints reduces the design space to only 122 feasible candidates. This sampling method results in 104 alloys that contain Cu and 18 that do not. The highest concentration of Cu in these 122 alloys is 70 at.%. This is important as we would like to probe the effect of Cu (and the lack of Cu) on the SFE of these systems.

Density-functional theory method for stacking-fault energy: The Green's function based DFT approach, i.e., Korringa-Kohn-Rostoker Method to Coherent Potential Approximation (KKR-CPA) (Singh et al., 2020; P. Singh et al., 2024), combined with axial next-nearest-neighbor Ising (ANNNI) model (Khan et al., 2022) was employed to calculate the SFE of arbitrary MPEAs. The KKR-CPA technique is a fully variational, exact DFT method, unlike historical tight-binding versions, and it can be extended beyond single-site average, if needed, using a cluster generalization of the CPA. The KKR-CPA permits the structural defect to be added to the crystal structure, and then concomitantly with the DFT charge self-consistency, an average is performed simultaneously over all configurations – not just for one selected representation. The ability of the KKR-CPA to account for arbitrary chemical compositions in a self-consistent manner provides superiority over the supercell approach that is limited by the size of the supercell used. Monkhorst–Pack *k*-point meshes with Perdew–Burke–Ernzerhof (PBE) exchange-correlation functional (Perdew et al., 1996) were used for Brillouin zone (BZ) integration using $30 \times 30 \times 30$ (*fcc*), $30 \times 30 \times 15$ (hexagonal closed-packed, *hcp*), and $30 \times 30 \times 10$ (double hcp, *dhcp*), respectively.

The stacking sequence in the ANNNI model with pairwise (Ising) interactions can be modeled as a one-dimensional crystal whose energetics are governed by pair interactions of extended ranges. The (intrinsic) SFE can be computed using the analytic energy-difference expression after mapping the stacking sequence along directions normal to the (111) plane in fcc (.. .. .. **A:B:C:A:B:C** .. .. ..), hcp (.. .. .. **A:B:A:B** .. .. ..), and dhcp ((.. .. .. **A:B:A:C:A:B:A:C** .. .. ..) crystals as

$$\gamma_{ISF} = \frac{E_{hcp} + 2E_{dhcp} - 3E_{fcc}}{A_{fcc}} \tag{1}$$

where, A_{fcc} is the stacking-fault area per atom in the (111) fcc plane. The DFT- calculated E_{hcp}, E_{dhcp}, and E_{fcc} correspond to the total energy-per-atom in the fcc, hcp, and dhcp crystal phases with an average over all atomic configurations for disordered alloys, respectively. The spin-polarized setting was used in all our calculations due to the presence of magnetic elements (Fe, Co, Cr, Ni, Mn) in MPEAs. Additionally, the DFT-KKR-CPA can directly address any defected crystal structure that provides an independent validation of ANNNI prediction of SFE using Eq. (1). Like ANNNI estimate, a supercell with and without a SF gives a direct SFE estimate as

Table 1
List of systems sampled to study the effect of Cu additions Cantor-based MPEAs.

Fe-Mn-Ni-Co-Cr-Mo	Fe-Ni-Co-Cr-Ti	Fe-Ni-Co-Cr-Al-Cu
Fe-Mn-Ni-Co-Cr-Nb	Fe-Ni-Co-Al-Ti	Fe-Ni-Co-Cr-Mo-Cu
Fe-Mn-Ni-Co-Al-Cu	Fe-Ni-Co-Cr-Mo	Fe-Ni-Co-Cr-Nb
Fe-Ni-Co-Ti	Fe-Ni-Co-Al-Cu	

$$\gamma_{ISF} = \frac{E_{SF} - E_{fcc}}{A_{fcc}} \tag{2}$$

where configurational averaging is performed for 1-atom fcc and an 11-atom intrinsic SF cell (i.e., 11 (111)-layers) rather than 2-atom hcp and 4-atom dhcp for an ANNNI model estimate. Notably, the KKR-CPA method considers all possible configurations to calculate final total energies of given alloys, which are then used to calculate SFE. Due to inclusion of all possible configuration, our Green's function based DFT-KKR-CPA approach provides more accurate account of total defect energetics compared. Therefore, unlike other DFT based method including plane-wave methods, we do not require to consider 10 or 20 configurations to estimate final defect energetics.

Solute-solution-strengthening: The reduced model for the zero-temperature shear yield-stress (Varvenne et al., 2016) was used as represented by an analytical equation governed by the stiffness constants (C_{ij}'s):

$$\tau_{y0} = 0.01785 \times \alpha^{-\frac{1}{3}} \overline{\mu} \left(\frac{1+\overline{\nu}}{1-\overline{\nu}}\right)^{\frac{4}{3}} \left[\frac{\sum_n c_n \Delta V_n^2}{\overline{b}^6}\right]^{\frac{2}{3}} \tag{3}$$

where α is the edge dislocation line tension parameter, $\overline{\mu}$ is the shear moduli, $\overline{\nu}$ is Poisson's ratio, c_n is the concentration of type n solute, ΔV_n is the misfit volume of type n solute, and $\overline{b}$ is the Burger's vector (Varvenne et al., 2016). The $\overline{\mu}$, $\overline{\nu}$, and $\overline{B}$ (bulk moduli) are related to C_{ij}'s by

$$\overline{\mu} = \sqrt{\frac{1}{2}\, C_{44}\, (C_{11} - C_{12})} \tag{4}$$

$$\overline{B} = (C_{11} + 2C_{12}) \tag{5}$$

$$\overline{\nu} = \frac{3\,\overline{B} - 2\overline{\mu}}{2\left(3\,\overline{B} + \overline{\mu}\right)} \tag{6}$$

DFT-calculated stiffness constants, elemental elastic parameters and alloy volumes were used to estimate the C_{ij}'s. The misfit volume was estimated from the rule of mixtures. The misfit volume was estimated from the rule of mixtures. Due to lack of data and reliable predictive models, the temperature dependence of elastic properties is ignored in this model. Albeit oversimplified, the approach is self-consistent and allows us to compare the yield strength for large number of alloys. Details on the derivation of the model can be found in Ref. (Varvenne et al., 2016).

At finite temperature and finite strain rate, standard thermal activation theory then leads to the predicted tensile yield stress as:

$$\sigma_{y0} = 3.06\, \boldsymbol{\tau}_{y0} \left[1 - \left(\frac{kT}{\Delta E_b} ln \frac{\dot{\epsilon_0}}{\dot{\epsilon}}\right)^{2/3}\right] \tag{7}$$

Here, 3.06 is the Taylor factor for isotropic fcc polycrystal strength controlled by edge dislocations, where $\dot{\epsilon_0}$ is an estimated strain rate, $\dot{\epsilon}$ is experimental strain rate, k is Boltzmann constant, T is temperature, ΔE_b is a typical energy barrier between the lower-energy initial state and the higher-energy transition state, and τ_{y0} is the zero-temperature flow stress. The alloys Poisson's ratio was calculated using rule of mixture (PR=$\sum_i c_i PR_i$) where c_i and PR_i are elemental chemistry and Poisson's ratio of elements (taken from experiments), which was utilized for elastic property and strength calculation.

Other DFT Method: The VASP pseudo-potential code was also employed for conducting electronic-structure calculations utilizing the projector augmented-wave method (Kresse et al., 1993, 1999). Perdue-Burke-Ernzerhof (PBE) exchange-correlation functionals were applied within the generalized gradient approximation (GGA). A Monte Carlo-based special quasi-random supercell method was utilized to generate random fcc structures of 108 atoms for $Ni_{60}Fe_5Cr_5Co_5Cu_5Mo_{20}$ and $Ni_{60}Fe_5Cr_5Co_5Nb_{25}$ alloys (Van De Walle et al., 2004). The structures underwent relaxation with an energy convergence criterion of 10^{-6} eV and force convergence criteria of 10^{-3} eV/Å. A gamma-centered Monkhorst-Pack scheme was employed to create a 3 × 3 × 3 mesh for self-consistent calculations.

3. Results and discussion

3.1. Section 1 – stacking-fault energy validation

Here, we compare the DFT calculated SFE with experimentally measured SFEs to validate the accuracy of DFT-predicted SFEs from higher order ANNNI model, as shown in Eq. (1). Notably, only positive SFEs can be inferred experimentally within 4 mJ/m^2. First, we determined the SFE of elemental solids, including Ni and Al, followed by Fe-Mn-Co-Cr-based MPEAs and steels. For elemental Ni and Al, the DFT-predicted SFE was 130 and 136 mJ/m^2, in good agreement with experiments, e.g., Ni (125 mJ/m^2 (Carter et al., 1977), Al (120–130 mJ/m^2; (Denteneer et al., 1991)). The SFE for FeMnCoCr solid solution is estimated as 17±4 mJ/m^2 (Picak et al., 2019), in good agreement with the ANNNI model (Eq. (1)) predicted SFE of 22.3 mJ/m^2. For NiCoCr, ANNNI-estimated SFE (20.7 from Eq. (1)) agrees with direct DFT SFE (18.5 mJ/m^2 from Eq. (2)) and experiments (22±4 mJ/m^2) (Picak et al., 2023).

In Fig. 2, we show the SFE calculated from ANNNI model in Eq. (1) (grey bars) for CALPHAD selected single phase 39 fcc MPEAs (V-Cr-Mn-Fe-Co-Ni-Al), while SFE values represented by asterisk (*) were calculated using lower order ANNNI model that does not include DHCP phase, i.e., axial nearest-neighbor Ising model instead of next-nearest neighbor. We found that the higher-order correction has a strong effect on SFE values. For example, MPEAs with higher SFEs show a much larger correction than MPEAs with low SFEs (-0.25 mJ/m^2 < SFE < 25 mJ/m^2). Negative SFE represents metastability in fcc structures, i.e., not in thermodynamic equilibrium. However, these metastable MPEAs under externally applied forces (e.g., tensile force) can develop TRIP and TWIP, respectively, which can provide additional strength and ductility and may counterbalance the strength-ductility trade-off (Ritchie et al. 2011; Lu et al., 2014; Ma et al., 2019, 2017; Li et al., 2016).

3.2. Section 2 - Cantor-based V-Cr-Mn-Fe-Co-Ni-Al MPEAs

The DFT-calculated SFE of 94 thermodynamically stable V-Cr-Mn-Fe-Co-Ni-Al MPEAs calculated using ANNNI-model is shown in Fig. 3. To understand the role of individual elements on SFE, in Fig. 3**a-f**, we plot the SFE values against two sets of elements, i.e., majority (Fe, Mn, Ni) constituents in Fig. 3**a-c**, and minority (Cr, Al, V) constituents in Fig. 3**d-f**. The inclusion of Cr and Al in this discussion is based on their pivotal role in providing oxidation resistance for high-temperature applications, while (Fe, Mn, and Ni) constitute readily available materials.

In Fig. 3**b**, we plot the Mn dependence of SFE as the excellent mechanical properties of Mn-rich alloys play a key role in structural components in the automobile industry. The mechanical performance depends on the plastic deformation mechanisms such as TWIP, TRIP, and/or dislocation glide (Luo et al., 2018), which directly connects to the key physical quantity, i.e., SFE, governing the deformation mechanism (Pierce et al., 2015, 2012). We found an increasing trend of SFE in Fig. 3**b** with increasing Mn content in MPEA, which is opposite to that of Fe in Fig. 3**a**. If we compare the Fe and Mn cases, the negative SFEs fall in the region of very high Fe content (>50 at% Fe). In Fig. 3**c**, we show the impact of Ni on SFE, which indicates a strong linear dependence on Ni content in V-Cr-Mn-Fe-Co-Ni-Al MPEA. Increasing Fe content at the cost of Mn/Ni notably leads to much-reduced SFEs. As shown before, Ni with a high Mn content leads to martensite transformation, while further increasing their content will lead to an increased proportion of acicular ferrite and micro-segregation in a network or parallel to grain boundaries (Kang et al., 2000). Also, we emphasize the role of Mn, an important SFE stabilizer element in steels and/or superalloys. However, the effect of Mn on SFE is very complicated compared to Ni or other host elements (Jaberi et al., 2012). Previously, first-principles studies have shown that Mn addition to stainless steel always decreases the SFE at 0 K (Das, 2016), while (Pierce et al., 2014) showed a monotonous increase in SFE for 22–28 wt.% Mn (or above) in steels. Here, in Fig. 3**b**, we found a different Mn dependence of SFE compared to Fe-Mn-based steels, attributed to the chemical complexity of MPEAs compared to a solute-based matrix.

In Fig. 3, we found a positive correlation between SFE and (Mn, Ni, V) while a negative correlation is seen for Fe. In contrast, SFE looks weakly correlated or uncorrelated with (Cr, Al) content, i.e., no significant change in SFE. The predicted correlation trends in Fig. 3 show good agreement with the report of (Zaddach et al., 2013), where they observed similar behavior of SFE with a change in Ni content. However, no major correlations were observed for other elements. Khan et al. attributed this to the automatic cancellation of negative or positive contributions of entropy to SFE of Fe, Ni, or other constituents, as no correlation was found between entropy and compositional complexity (Khan et al., 2022).

Stacking-fault energy: Lu et al. (Lu et al., 2011) have shown that refractory elements such as Nb (near 3 at.%) have a strong effect on the SFE of the Fe-Cr-Ni system (Pierce et al., 2014). However, the systematic understanding of refractory (Nb, Ta, Mo, W) addition on the SFE of MPEAs is still lacking. In Fig. 4**a-l**, we plot the DFT-calculated SFEs with respect to (Fe, Mn, Ni) composition for refractory-reinforced MPEAs where refractory content is fixed at 5 at.%. The 5 at.% refractory content was proportionally balanced to

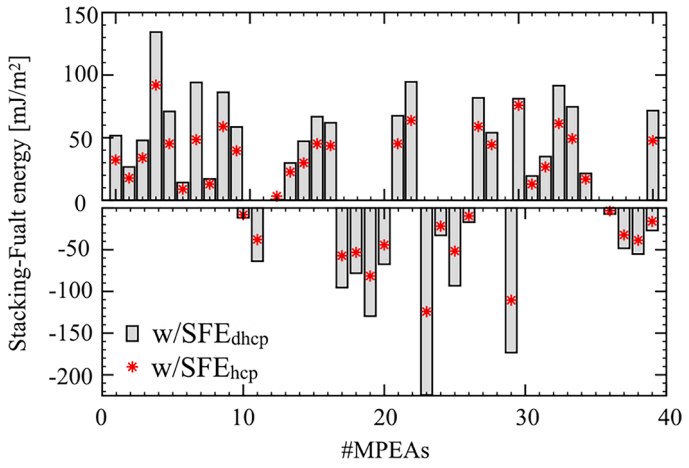

Fig. 2. Comparing SFE of 39 MPEAs calculated using ANNNI model (Eq. (1), grey bars) and model ignoring higher-order corrections, i.e., $\frac{2E_{hcp}-2E_{fcc}}{A_{fcc}}$, i.e., ignoring the *dhcp* correct terms.

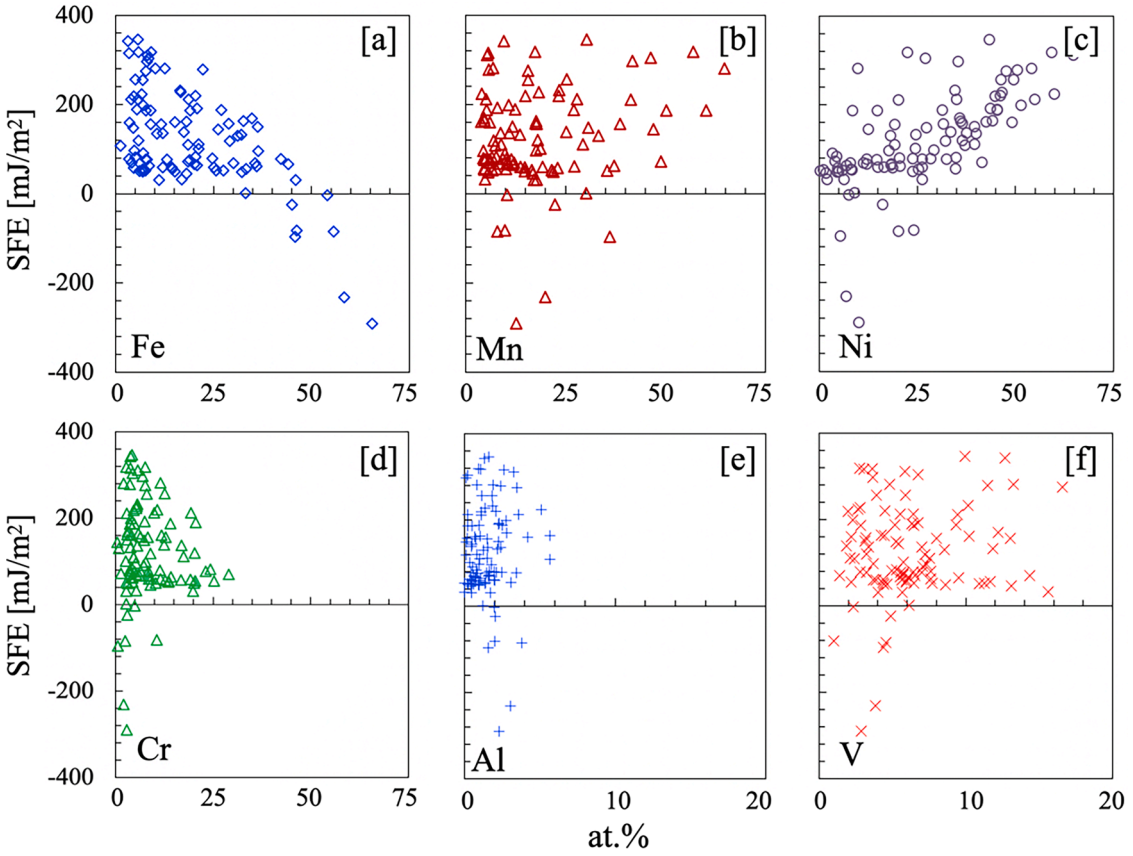

Fig. 3. Element-specific SFE and its dependence on their content in V-Cr-Mn-Fe-Co-Ni-Al: (a) 0 – 70 at.%Fe, (b) 0 – 70 at.%Mn, (c) 0 – 70 at.%Ni, (d) 0 – 30 at.%Cr, (e) 0 – 5 at.%Al, and (f) 0 – 17 at.%V.

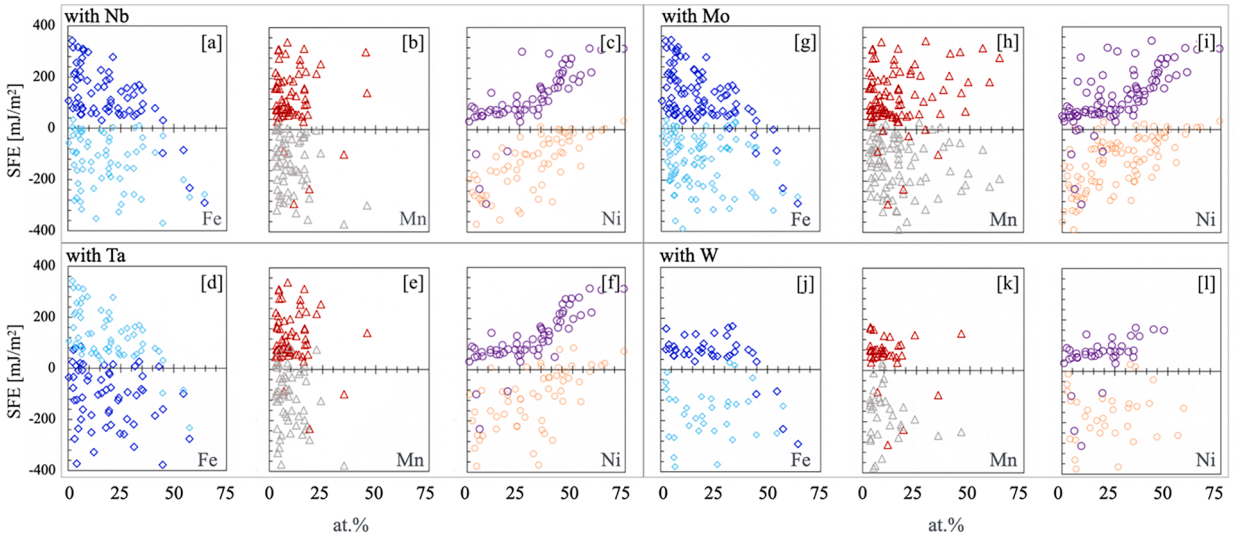

Fig. 4. The DFT-calculated stacking fault energy of refractory reinforced V-Cr-Mn-Fe-Co-Ni-Al-X MPEAs for (a-c) *X*=Nb, (d-f) *X*=Ta, (g-i) *X*=Mo, and (j-l) *X* = *W* with respect to Fe, Mn, and Ni composition. The refractory content is fixed at 5 at.% in MPEAs.

each alloying element in V-Cr-Cr-Mn-Fe-Co-Ni MPEAs.

In Fig. 4**a-l**, we have shown SFE variation with respect to Fe, Mn, Ni in V-Cr-Cr-Mn-Fe-Co-Ni MPEAs due to chemical alloying by refractory elements, i.e., Nb, Ta, Mo, and W. Notably, even a small amount of refractory addition shows strong effect on SFE, which

completely changed the correlation seen in Fig. 3**a** (Fe) and Fig. 3**c** (Ni) for refractory free MPEAs. In Fig. 4**a,d,g**, the SFE trends at higher Fe do not change much, but the low Fe region shows an order of magnitude change in SFE. On the other hand, Ni was highly correlated to SFE, as shown in Fig. 4**i**. However, this behavior fundamentally transforms and shows weak dependence on Ni composition on the inclusion of 5 at.% refractory elements. This suggests that SFE in fcc MPEAs are strongly amenable to refractory content in a particular way, providing greater control in achieving MPEAs with designer SFEs.

To understand the underlying origin of such change in SFE, we analyzed the correlation of SFE with different elemental properties (see supplemental **Fig. S1** and **Fig. S2**), including electronegativity variance ($\Delta\chi_{variance}$), valence-electron count (VEC), size effect for metallic ($\delta_{metallic}$) and covalent radii ($\delta_{covalent}$), Pugh's ratio (PR), DOS at Fermi level (DFT), equilibrium volume change (ΔV_0; DFT-elemental average), variance in heat of fusion ($\Delta HF_{variance}$) and electron affinity ($\Delta EA_{variance}$). Notably, we found a positive correlation between SFE and $\Delta EA_{variance}$ (see **Fig. S1**) This indicates that $\Delta EA_{variance}$ a good indicator of controlling SFE by maximizing bonding strength through chemical tuning in MPEAs. We found that a subtle alteration in electronegativity and covalency resulting from refractory alloying can significantly impact the plasticity of fcc MPEAs.

Temperature-dependence of yield strength: The yield strength is a critical mechanical feature when designing high-performance materials. We used Curtin's solid-solution-strengthening model to evaluate the yield strength of MPEAs (Varvenne et al., 2016). In Fig. 5**a-f** (X=Mo, W) and Fig. 5**g-l** (X=Nb, Ta), we show the temperature dependence of model predicted yield-strength at 300 K, 500 K, and 900 K for V-Cr-Mn-Fe-Co-Ni-Al-X MPEAs. The model predictions are validated for selected refractory MPEAs in supplemental **Fig. S6**, which shows good agreement with experiments (Senkov et al., 2011).

The temperature dependence of strength is shown with respect to the chemical variation of Fe, Mn, and Ni in MPEAs. In Fig. 5, predicted strength shows systematic decreases with an increase in temperature from RT, 500 K, and 900 K. This range for various refractories is as follows: 0.7 GPa to 0.25 GPa for Mo, 0.75 GPa to 0.30 GPa for W, 0.87 GPa to 0.40 GPa for Nb, and 0.92 GPa to 0.45 GPa for Ta, respectively. Notably, in Fig. 5**c-j**, the increase in Ni contents shows a near-linear increase in strength while it negatively correlates to the compositional increase of Fe and Mn. The higher strength of Ni-rich alloys is attributed to the formation of strong directional bonds between Ni-d and Al-p, which also plays a significant role in determining shear modulus in MPEAs (Jeong et al., 2023). Contrasted to our moduli analysis in **Fig. S3–5**, strength decreases as a function of Fe in Fig. 5 (top panel). However, MPEAs with higher refractory metals consistently appear in the higher-strength range. This further establishes a correlation between moduli and strength.

3.3. Section 3 – effect of Mo and Cu composition on SFE tunability

Stacking-fault energy: In Fig. 6**a-c**, we show the SFE for varying Mo, Mn, and Cu composition in 122 CALPHAD down-selected Cr-Mn-Fe-Co-Ni-Ti-Al-Cu-Mo MPEAs. In contrast to the 5 at.% Mo addition in Fig. 3**g-i**, we varied Mo from 0 to 25 at.% in Fig. 6**a**, while Mn (Fig. 6**b**) and Cu (Fig. 6**c**) were varied from 0 to 30 at.% and 0–70 at.%, respectively. The Mn in Fig. 6**b** shows no systematic change in SFE in nine-component Cr-Mn-Fe-Co-Ni-Ti-Al + Cu-Mo MPEAs. On the other hand, Mo in Fig. 6**a** shows a systematic decrease of SFEs,

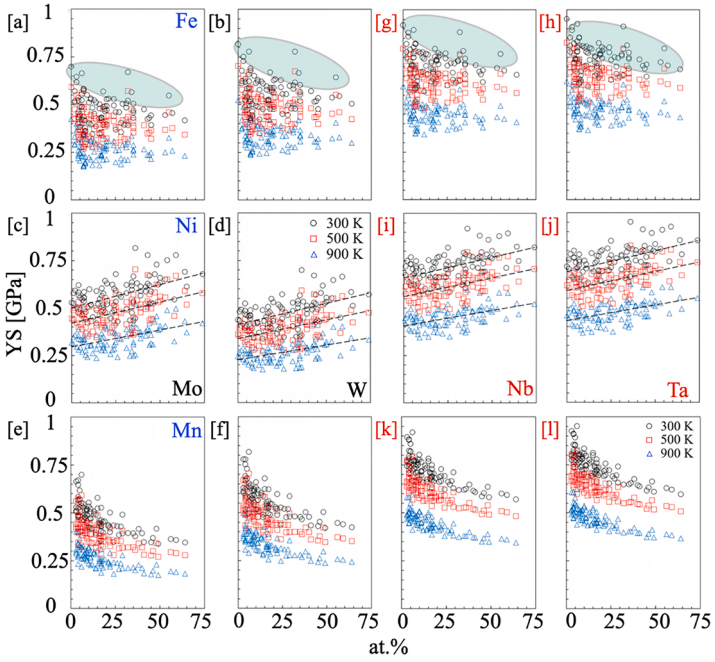

Fig. 5. Predicted yield-strength of V-Cr-Mn-Fe-Co-Ni-Al + X MPEAs at 300 K, 500 K, and 900 K, where refractory elements, i.e., X= Mo, W (a-f), and Nb, Ta (g-l), are fixed at 5 at%.

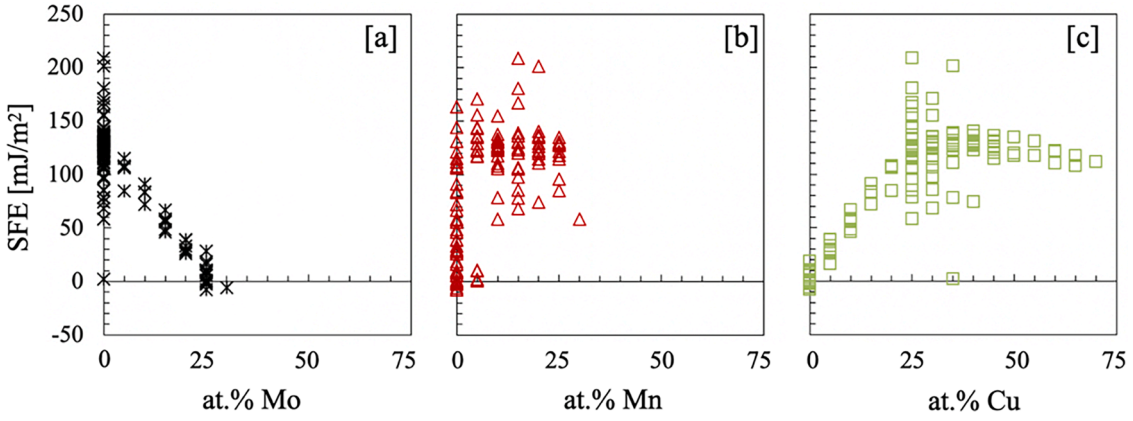

Fig. 6. DFT calculated SFE dependence on (a) Mo, (b) Mn, and (c) Cu at.% change is shown for 122 CALPHAD selected single phase Cr-Mn-Fe-Co-Ni-Ti-Al-Cu-Mo based MPEAs.

which goes to zero near 25 at.% Mo at fixed total concentration of Mn and Cu. In contrast, SFE with respect to Cu in Fig. 6**c** shows a systematic increase up to 35 at.% with strong deviation in SFE at 25 and 30 at.%. of Cu, which occurs at 0 and 25 at.% Mo. However, further addition of Cu has no significant impact on SFE, which indicates the solubility limit or saturation range of Cu. Our findings point towards pronounced tunability of SFE with respect to Mo, whereas Cu and Mn exhibit weaker variation.

In supplemental **Fig. S7**, we analyzed and plotted the correlation of SFE with $\Delta\chi_{variance}$ and $\delta_{covalent}$ (**Fig. S7b,d**), where we found that lower variance in electronegativity and size-effect drive higher SFE. In **Fig. S7b, d**, we have shown a correlation between higher {VEC and $\Delta EA_{variance}$} with higher SFE. This suggests a strong correlation between SFE and alloy features in presence of refractory elements, which shows that addition of refractory elements provide higher SFE tunability in fcc MPEAs.

Temperature dependence of yield strength: In Fig. 7, we plot model predicted strength versus Mo, Mn, and Cu for Cr-Mn-Fe-Co-Ni-Ti-Al-Cu-Mo MPEAs, showing a systematic decrease with temperature increase from RT, 500 K, and 900 K. The observed trends in strength corroborate DFT-calculated moduli trends in **Fig. S8**, which further establishes a strong correlation between intrinsic mechanical quantities with yield strength. On the other hand, comparing mechanical properties in **Fig. S8** and Fig. 7 with SFE in Fig. 6 shows a clear trade-off between refectory concentration and SFE-strength in FCC MPEAs.

3.4. Section 4 - CALPHAD+DFT-predicted MPEAs with optimal SFE and strength

We combined DFT-predicted SFE and other elastic properties including intrinsic strength (bulk moduli) to down-select the best performing MPEAs as shown in Table 2, (also see **Fig. S10**). The magnitude of SFE has been a good qualifier to predict the type of deformation mechanism (TWIP or TRIP) in fcc alloy (Khan et al., 2022), which contributes towards the ductility of fcc alloys (Chaudhary et al., 2017). For example, the SFE value in the range of 15 mJ/m^2 < SFE < 30 mJ/m^2 has been found to enhance the likelihood of promoting the TRIP and/or TWIP mechanisms (Lu et al., 2016).

The correlation between DFT calculated SFEs vs. other elastic properties and yield strength for a subset of the dataset (Mo-based alloys) is shown in the appendix **Fig. S10.** The goal of analyzing the correlation between SFE and other mechanical properties, such as strength and elastic moduli (E/G/B), was to find the best compositions that show optimal SFE (15 mJ/m^2 < SFE < 30 mJ/m^2) with superior elastic properties. For refractory reinforced compositions with SFE >0 (see shaded region in **Fig. S10**), we found very few MPEAs that show optimal SFE (15 mJ/m^2 < SFE < 30 mJ/m^2) critical for TWIP/TRIP behavior including superior mechanical characteristics with higher range of Bulk-moduli (B > 150 GPa), shear-moduli (G > 75 GPa), Young's-moduli (E > 200 GPa), yield-strength (YS> 250 MPa for Mo-based MPEAs; and >950 MPa for Nb-based MPEAs at 900 K)}, ductility (Pugh's ratio), and solidus

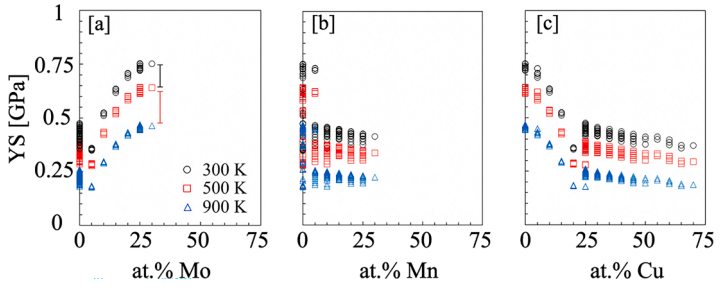

Fig. 7. Effect of compositional tuning by (a) Mo, (b) Mn, and (c) Cu on predicted yield-strength of Cr-Mn-Fe-Co-Ni-Ti-Al-Cu-Mo MPEAs at 300 K, 500 K, and 900 K. The effect of other refectories on yield-strength is shown in supplemental Fig. S9.

Table 2
DFT predicted SFEs, elastic properties (B/G/E), yield-strength (at 900 K), and ductility (Pugh's ratio; PR; ductile >1.8), and solidus temperature (see **Fig. S14**) of selected set of eight refractory reinforced Ni-rich MPEAs. The phase stability analysis of selected set on given alloy composition space was done at 1300 K and 300 K using CALPHAD as shown in **Fig. S12 &S13**.

MPEAs	Compositions	SFE mJ/m^2	B GPa	G	E	YS [900 K] MPa	PR	Solidus K
MPEA1	$Ni_{21}Fe_{35}Cr_4Co_4Mn_{26}V_3Al_2Mo_5$	28.4	159.6	80.5	208.6	237.5	2.0	1341.7
MPEA2	$Ni_{39}Fe_{35}Cr_3Co_3Mn_{11}V_2Al_2Mo_5$	21.9	169	80.2	208.3	264.5	2.12	1367.1
MPEA3	$Ni_{74}Fe_2Cr_4Co_5Mn_5V_2Al_3Mo_5$	33.8	175	78	205	331.3	2.27	1286.8
MPEA4	$Ni_{60}Fe_5Cr_5Co_5Cu_5Mo_{20}$	38.5	186	87	227	430.1	2.12	1633.9
MPEA5	$Ni_{50}Fe_5Cr_5Co_{15}Cu_5Nb_{20}$	25.8	186.5	86.9	228.2	972	2.15	1611.7
MPEA6	$Ni_{55}Fe_5Cr_{10}Co_5Cu_5Nb_{20}$	28.1	185.5	88.9	231.2	976	2.03	1607.4
MPEA7	$Ni_{55}Fe_5Cr_5Co_5Cu_5Nb_{25}$	28.5	189	89.6	233.7	1041	2.11	1608.1
MPEA8	$Ni_{60}Fe_5Cr_5Co_5Nb_{25}$	18.3	191	90.9	237.2	1069	2.33	1684.1

temperature (>1300 K, see **Fig. S8**) was applied for final downs-election of eight MPEAs. We have also analyzed the higher order correlation required to calculate SFE in **Fig. S11**, where interestingly, we found that diminished higher-order interaction parameters $\{J_1, J_2\}$ in case of down-selected MPEAs with positive SFEs, which is in contrasts with simple metals such as elemental solids. The energy map in **Fig. S11** can be useful in determining phase stability of complex MPEAs.

Finally, the solidus temperature of eight down-selected MPEAs was calculated using nonequlibrium Scheil model as implemented within CALPHAD framework. Notably, only Nb-rich alloys (Nb~20–25 at.%), in **Table 2** show much-improved strength-ductility trade-off while only minor Mo-based MPEAs were found with favorable SFE (15 mJ/m^2 < SFE < 30 mJ/m^2). The phase stability for some of these alloy spaces was also assessed using CALPHAD, which are shown in **Fig. S12** and **Fig. S13**.

3.5. Section 5 - Electronic structure of Mo-rich $Ni_{60}Fe_5Cr_5Co_5Cu_5Mo_{20}$ and Nb-rich $Ni_{60}Fe_5Cr_5Co_5Nb_{25}$ MPEAs

The impact of element composition on structural properties is elucidated by analyzing the electronic structure of the MPEA4 and MPEA8 from Table 2. The reason for this choice is based on similar refractory composition. The introduction of Nb replacing {Mo, Cu} in MPEA4 (Table 2) leads to an augmented bonding where Nb-rich alloys show 0.3 % reduced average bond length in the immediate Nb neighborhood. The stronger bond strength arises from increased hybridization of Nb atoms with Cr, Co, and Fe, as evidenced by the overlap of *d* states observed in the partial density of states shown in Fig. 8**a&b** (see the zoomed DOS plot in supplementary **Fig. S15**). The Cu *4d* states exhibit a slightly displaced peaks compared to other elements in Fig. 8**a**, indicating a potentially detrimental effect of Cu on bonding, resulting in diminished mechanical properties compared to MPEA8, which shows much-improved strength. The shrinking of bond length could also be attributed to increased charge sharing due to the higher electronegativity difference of Nb with its surroundings that leads to increased strength of Nb-rich alloys [MPEA5-MPEA8] compared to Mo-based alloys [MPEA1-MPEA4].

In Fig. 8**c&d**, the differential charge distribution between the two MPEAs is illustrated, highlighting the influence of the higher electronegativity of Nb compared to {Mo, Cu} in reinforcing change in bonding. Replacing {Mo (VEC=6), Cu (VEC=11)} with Nb (VEC=5) is equivalent to adding 0.5 holes that lead to complete charge rearrangement around Nb, forming stronger bonds, as discussed in the context of the density of states. The Nb/Mo sites (red spheres in Fig. 8**d**) reflect enhanced charge activity with neighboring atoms. Our observation that changes in charge rearrangement going from Mo to Nb-based alloys directly correlate with strength underscores the significance of enhanced bonding effect and electronic structure on mechanical properties of refractory reinforced fcc MPEAs.

4. Conclusion

In this work, we employed CALPHAD, DFT, and strength models to carefully investigate the role of varying chemistry of refractory elements and Cu on the SFEs and strength of FCC V-Cr-Mn-Fe-Co-Ni-Al MPEAs. We show that even a slight addition of refractories strongly affects SFE of FCC alloys, which can further be modified by tuning high VEC metals like copper. Theoretical and experimental evidence exists that the SFE can be used to infer the likelihood of deformation mechanisms, such as TRIP or TWIP, for example, the SFE of around 20 mJ/m^2 was found to produce desired TRIP and TWIP-based deformation mechanisms, therefore, contributors to the ductility in FCC alloy. Interestingly, we discovered several MPEAs satisfying the target criteria of ~20 mJ/m^2, which is promising to activate additional plasticity mechanisms and increase their ductility and overcome the strength-ductility trade-off. The new compositions with the desired range of SFE found here will provide a material design guide for experimentalists toward achieving materials with improved plasticity. Additionally, Ni-rich MPEAs, with no refractory metals, show the most pronounced effect and increasing trends in SFE regardless of the content of other host elements. We believe that our study will allow to understand and control the influence of chemical alloying by refractory metals on SFE of chemically complex FCC alloys, which will enable the design of high-performance FCC alloys with improved plasticity and strength.

CRediT authorship contribution statement

Prashant Singh: Writing – review & editing, Writing – original draft, Visualization, Validation, Supervision, Software, Resources,

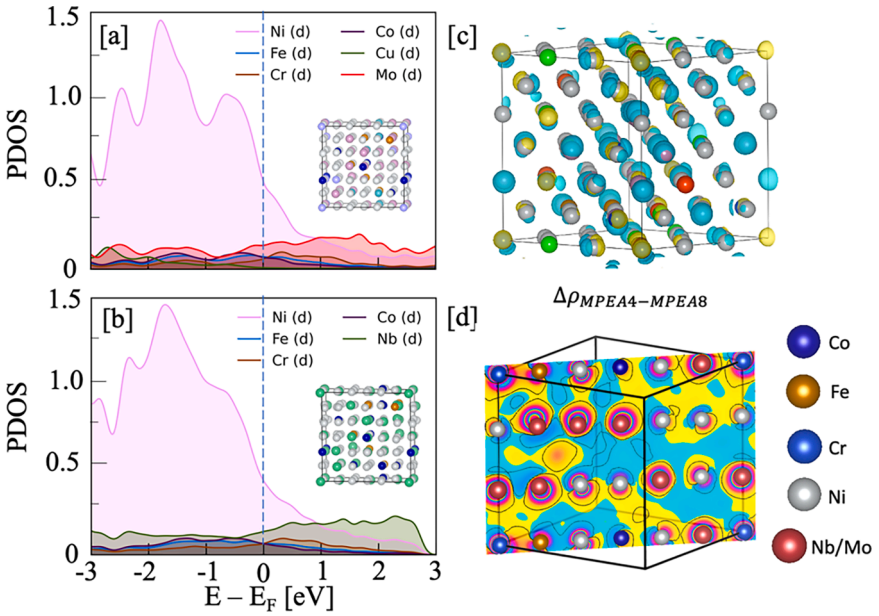

Fig. 8. Comparative analysis of the partial density of states for (a) MPEA4-$Ni_{60}Fe_5Cr_5Co_5Cu_5Mo_{20}$ and (b) MPEA8-$Ni_{60}Fe_5Cr_5Co_5Nb_{25}$. Additionally, (c) illustrates the charge difference between MPEA4 and MPEA8, while (d) provides a 2D slice of the charge difference on the refractory rich plane.

Project administration, Methodology, Investigation, Funding acquisition, Formal analysis, Data curation, Conceptualization. **William Trehern:** Writing – review & editing, Methodology, Data curation. **Brent Vela:** . **Prince Sharma:** Writing – review & editing, Visualization, Methodology, Investigation, Formal analysis, Data curation. **Tanner Kirk:** Writing – review & editing, Software, Methodology, Investigation, Formal analysis, Data curation. **Zongrui Pei:** Writing – review & editing, Formal analysis, Data curation. **Raymundo Arroyave:** Writing – review & editing, Supervision, Funding acquisition. **Michael C. Gao:** Writing – review & editing, Supervision, Funding acquisition, Conceptualization. **Duane D. Johnson:** Writing – review & editing, Supervision.

Declaration of competing interest

The authors declare that they have no known competing financial interests or personal relationships that could have appeared to influence the work reported in this work.

Data availability

Data will be made available on request.

Acknowledgment

The work at Ames National Laboratory was supported by the U.S. Department of Energy, Office of Science, Basic Energy Sciences, Materials Science and Engineering Division. The research is performed at the Ames National Laboratory, which is operated for the U.S. DOE by Iowa State University under contract DE-AC02–07CH11358. BV acknowledges the support of NSF through Grant No. DGE-1545403 and acknowledges support from NSF through Grant No. 1746932. RA also acknowledges NSF through Grant No. 2119103. PSh acknowledges the support from NSF through Grant No. 1944040. PS acknowledges Funding support in part (analyzing the role of refractory metals) from the Laboratory Directed Research and Development (LDRD) program at Ames National Laboratories. WT and MCG acknowledge the support of the U.S. Department of Energy's Fossil Energy and Carbon Management through the NETL Research and Innovation Center's Advanced Materials Development Field Work Proposal. We thank Ryan Ott of Ames National Laboratory for providing access to ThermoCalc software, which was used for phase stability and solidus temperature simulation.

Supplementary materials

Supplementary material associated with this article can be found, in the online version, at doi:10.1016/j.ijplas.2024.104020.

References

Anderson, P.M., Hirth, J.P., Lothe, J., 2017. Theory of Dislocations. Cambridge University Press, Oxford.

Carter, C.B., Holmes, S.M., 1977. The stacking-fault energy of nickel. Philos. Mag. 35 (5), 1161–1172.

Chang, X., Zeng, M., Liu, K., Fu, L., 2020. Phase engineering of high-entropy alloys. Adv. Mater. 32, 1–22. https://doi.org/10.1002/adma.201907226.

Chaudhary, N., Abu-Odeh, A., Karaman, I., Arróyave, R., 2017. A data-driven machine learning approach to predicting stacking faulting energy in austenitic steels. J. Mater. Sci. 52 (18), 11048–11076.

Chen, H.L., Mao, H., Chen, Q., 2018. Database development and CALPHAD calculations for high entropy alloys: challenges, strategies, and tips. Mater. Chem. Phys. 210, 279–290.

Chen, W., Hilhorst, A., Bokas, G., et al., 2023. A map of single-phase high-entropy alloys. Nat. Commun. 14, 2856.

Das, A., 2016. Revisiting Stacking Fault Energy of Steels. Metall Mater Trans A Phys Metall Mater Sci 47, 748–768.

Deng, Y., et al., 2015. Design of a twinning-induced plasticity high entropy alloy. Acta Mater. 94, 124–133.

El-Atwani, O., et al., 2019. Outstanding radiation resistance of tungsten-based high-entropy alloys. Sci. Adv. 5, eaav2002.

Freund, L.P., et al., 2017. Segregation assisted microtwinning during creep of a polycrystalline L12-hardened Co-base superalloy. Acta Mater. 123, 295–304.

Gao, M.C., Yeh, J.-W., Liaw, P.K., Zhang, Y., 2016. High-Entropy Alloys Fundamentals and Applications. Springer.

George, E.P., Raabe, D., Ritchie, R.O., 2019. High-entropy alloys. Nat. Rev. Mater. 4, 515–534. https://doi.org/10.1038/s41578-019-0121-4.

George, E.P., Curtin, W.A., Tasan, C.C., 2020. High entropy alloys: a focused review of mechanical properties and deformation mechanisms. Acta Mater. 188, 435–474.

Grässel, O., Krüger, L., Frommeyer, G., Meyer, L.W., 2000. High strength Fe-Mn-(Al, Si) TRIP/TWIP steels development—Properties—Application. Int. J. Plast. 16, 1391–1409.

Huang, S., et al., 2018. Twinning in metastable high-entropy alloys. Nat. Commun. 9 (1), 1–7.

Jaberi, F.S., Kokabi, A.H., 2012. Effect of nickel additions on microstructure evolution and mechanical properties of low-alloy Cr-Mo cast steel. J. Mater. Eng. Perform 2, 1447–1454.

Jeong, I.-S., Lee, J.-H., 2023. Single-phase lightweight high-entropy alloys with enhanced mechanical properties. Mater. Des. 227, 111709.

Jia, Z., et al., 2021. A self-supported high-entropy metallic glass with a nanosponge architecture for efficient hydrogen evolution under alkaline and acidic conditions. Adv. Funct. Mater. 31 (38), 2101586.

Kang, B.Y., Kim, H.J., Hwang, S.K., 2000. ISIJ Int. 40, 1237–1245.

Khan, T., et al., 2022. Towards Stacking Fault Energy Engineering in FCC High Entropy Alloys. Acta Mater. 224, 117472.

Kim, J.-K., et al., 2022. Temperature-dependent universal dislocation structures and transition of plasticity enhancing mechanisms of the Fe40Mn40Co10Cr10 high entropy alloy. Int. J. Plast. 148, 103148.

Kresse, G., Hafner, J., 1993. Ab initio molecular dynamics for liquid metals. Phys. Rev. B 47, 558–561.

Kresse, G., Joubert, D., 1999. From ultrasoft pseudopotentials to the projector augmented-wave method. Phys. Rev. B 59, 1758–1775.

Le, L., et al., 2022. Tensile and compressive plastic deformation behavior of medium-entropy Cr-Co-Ni single crystals from cryogenic to elevated temperatures. Int. J. Plast. 148, 103144.

Li, Z., Tasan, C.C., Pradeep, K.G., Raabe, D., 2017. A TRIP-assisted dual-phase high- entropy alloy: grain size and phase fraction effects on deformation behavior. Acta Mater. 131, 323–335.

Li, L., et al., 2023. Plastic deformation of single crystals of the equiatomic Cr-Fe-Co-Ni medium entropy alloy – A comparison with Cr-Mn-Fe-Co-Ni and Cr-Co-Ni alloys. Int. J. Plast. 169, 103732.

Liu, S., et al., 2019. Transformation-reinforced high-entropy alloys with superior mechanical properties via tailoring stacking fault energy. J. Alloys Compd. 792, 444–455.

Lu, K., 2014. Making strong nanomaterials ductile with gradients. Science 345, 1455–1456.

Li, Z., Pradeep, K.G., Deng, Y., Raabe, D., Tasan, C.C., 2016. Metastable high-entropy dual-phase alloys overcome the strength-ductility trade-off. Nature 534, 227–230.

Luo, Z.C., Liu, R.D., Wang, X., Huang, M.X., 2018. The effect of deformation twins on the quasi-cleavage crack propagation in twinning-induced plasticity steels. Acta Mater. 150, 59–68.

Lu, S., Hu, Q.-M., Johansson, B., Vitos, L., 2011. Stacking fault energies of Mn, Co and Nb alloyed austenitic stainless steels. Acta Mater. 59, 5728–5734.

Lu, J., Hultman, L., Holmström, E., et al., 2016. Stacking fault energies in austenitic stainless steels. Acta Mater. 111, 39–46.

Ma, E., Wu, X., 2019. Tailoring heterogeneities in high-entropy alloys to promote strength–ductility synergy. Nat. Commun. 10, 5623.

Ma, E., Zhu, T., 2017. Towards strength–ductility synergy through the design of heterogeneous nanostructures in metals. Mater. Today 20, 323–331.

Makineni, S.K., et al., 2018. On the diffusive phase transformation mechanism assisted by extended dislocations during creep of a single crystal CoNi-based superalloy. Acta Mater. 155, 362–371.

Mao, H., Chen, H.L., Chen, Q., 2017. TCHEA1: a thermodynamic database not limited for high entropy alloys. J. Phase Equilib. Diffus. 38 (4), 353–368.

Miracle, D.B., Senkov, O.N., 2017. Critical review of high entropy alloys and related concepts. Acta Mater. 122, 448–511. https://doi.org/10.1016/j.actamat.2016.08.081.

Otto, F., Yang, Y., Bei, H., George, E.P., 2013. Relative effects of enthalpy and entropy on the phase stability of equiatomic high-entropy alloys. Acta Mater. 61, 2628–2638. https://doi.org/10.1016/j.actamat.2013.01.042.

Ouyang, G., et al., 2023. Design of refractory multi-principal-element alloys for high-temperature applications. NPJ Comput. Mater. 9, 141.

Ouyang, G., et al., 2024. Predictive design of novel nickel-based superalloys beyond Haynes 282. Acta Mater. 120045 https://doi.org/10.1016/j.actamat.2024.120045.

Perdew, J.P., Burke, K., Ernzerhof, M., 1996. Generalized gradient approximation made simple. Phys. Rev. Lett. 77 (18), 3865.

Picak, S., et al., 2019. Anomalous work hardening behavior of $Fe_{40}Mn_{40}Cr_{10}Co_{10}$ high entropy alloy single crystals deformed by twinning and slip. Acta Mater. 181, 555–569.

Picak, S., et al., 2023. Orientation dependence of the effect of short-range ordering on the plastic deformation of a medium entropy alloy. Mater. Sci. Eng. A 888, 145309.

Pierce, D.T., Jiménez, J.A., Bentley, J., Raabe, D., Wittig, J.E., 2015. The influence of stacking fault energy on the microstructural and strain-hardening evolution of Fe-Mn-Al-Si steels during tensile deformation. Acta Mater. 100, 178–190.

Pierce, D.T., Bentley, J., Jiménez, J.A., Wittig, J.E., 2012. Stacking fault energy measurements of Fe–Mn–Al–Si austenitic twinning-induced plasticity steels. Scr. Mater. 66, 753–756.

Pierce, D.T., et al., 2014. The influence of manganese content on the stacking fault and austenite/ε-martensite interfacial energies in Fe–Mn–(Al–Si) steels investigated by experiment and theory. Acta Mater. 68, 238–253.

Praveen, S., Kim, H.S., 2018. High-entropy alloys: potential candidates for high-temperature applications-an overview. Adv. Eng. Mater. 20 (1), 1700645.

Rao, Y., Smith, T.M., Mills, M.J., Ghazisaeidi, M., 2018. Segregation of alloying elements to planar faults in γ'-Ni_3Al. Acta Mater. 148, 173–184.

Ritchie, R.O., 2011. The conflicts between strength and toughness. Nat. Mater. 10, 817–822.

Senkov, O.N., Wilks, G.B., Scott, J.M., Miracle, D.B., 2011. Mechanical properties of $Nb_{25}Mo_{25}Ta_{25}W_{25}$ and $V_{20}Nb_{20}Mo_{20}Ta_{20}W_{20}$ refractory high entropy alloys. Intermetallics 19, 698–706.

Senkov, O.N., Miracle, D.B., 2016. A new thermodynamic parameter to predict formation of solid solution or intermetallic phases in high entropy alloys. J. Alloy. Compd. 658, 603–607.

Shi, P., et al., 2019. Enhanced strength-ductility synergy in ultrafine-grained eutectic high- entropy alloys by inheriting microstructural lamellae. Nat. Commun. 10, 1–8.

Singh, P., et al., 2020. Vacancy-mediated complex phase selection in high entropy alloys. Acta Mater. 194 (1), 540–546.
Singh, P., et al., 2024a. Theory-Guided design of duplex-phase multi-principal-element alloys. Acta Mater. 272, 119952 https://doi.org/10.1016/j.actamat.2024.119952.
Singh, P., et al., 2024b. Alloying effects on the transport properties of refractory high-entropy alloys. Acta Mater. 120032 https://doi.org/10.1016/j.actamat.2024.120032.
Singh, P., Picak, S., Sharma, A., Chumlyakov, Y., Arroyave, R., Karaman, I., Johnson, D.D., 2021. Martensitic transformation in high-entropy alloy. Phys. Rev. Lett. 127, 115704.
Suzuki, H., et al., 1952. Chemical interaction of solute atoms with dislocations. Sci. Rep. Res. Inst. Tohoku Univ. Ser. A Phys. Chem. Metall. 4, 455–463.
Suzuki, H., 1962. Segregation of solute atoms to stacking faults. J. Phys. Soc. Jpn. 17, 322–325.
Tsai, M.-H., Yeh, J.-W., 2014. High-entropy alloys: a critical review. Mater. Res. Lett. 2, 107–123. https://doi.org/10.1080/21663831.2014.912690.
Tsao, T.K., et al., 2017. The high temperature tensile and creep behaviors of high entropy superalloy. Sci. Rep. 7 (1), 12658.
Van De Walle, A., Asta, M., Ceder, G., 2004. The alloy theoretic automated toolkit: a user guide. Calphad 26, 539–553.
Varvenne, C., Luque, A., Curtin, W.A., 2016. Theory of strengthening in fcc high entropy alloys. Acta Mater. 118, 164–176.
Wagner, C., Laplanche, G., 2023. Effect of grain size on critical twinning stress and work hardening behavior in the equiatomic CrMnFeCoNi high-entropy alloy. Int. J. Plast. 166, 103651.
Wei, D., et al., 2022. Si-addition contributes to overcoming the strength-ductility trade-off in high-entropy alloys. Int. J. Plast. 159, 103443.
Wu, Z., et al., 2014. Temperature dependence of the mechanical properties of equiatomic solid solution alloys with face-centered cubic crystal structures. Acta Mater. 81, 428–441.
Xu, W.W., et al., 2022. Atomic origins of the plastic deformation micro-mechanisms of γ/γ' FeCoNiAlTi high-entropy alloys. Int. J. Plast. 158, 103439.
Yan, X., Zhang, Y., 2020. Functional properties and promising applications of high entropy alloys. Scripta Mater. 187, 188–193.
Yin, Y., et al., 2021. A cost-effective Fe-rich compositionally complicated alloy with superior high-temperature oxidation resistance. Corros. Sci. 180, 109190 https://doi.org/10.1016/j.corsci.2020.109190.
Zaddach, A., Niu, C., Koch, C., Irving, D., 2013. Mechanical properties and stacking fault energies of NiFeCrCoMn high-entropy alloy. JOM 65 (12), 1780–1789.
Zaretsky, E.B., Kanel, G.I., Razorenov, S.V., Baumung, K., 2005. Impact Engineering Impact strength properties of nickel-based refractory superalloys at normal and elevated temperatures. Int. J. Impact Eng. 31, 41–54.
Denteneer, P., Soler, J., 1991. Energetics of point and planar defects in aluminium from first-principles calculations. Solid State Commun. 78 (10), 857–861.
Zhao, Y., et al., 2006. Tailoring stacking fault energy for high ductility and high strength in ultrafine grained cu and its alloy. Appl. Phys. Lett. 89 (12), 121906.
Zhou, Y., et al., 2018. Design of non-equiatomic medium-entropy alloys. Sci. Rep. 8, 1236.